Appl. Phys. B 89, 129–140 (2007)
DOI: 10.1007/s00340-007-2753-0

Applied Physics B
Lasers and Optics

K.K. VENKATESAN[1,✉]
J. ZHANG[1]
G.B. KING[1]
N.M. LAURENDEAU[1]
M.W. RENFRO[2]

Hydroxyl space-time correlation measurements in partially premixed turbulent opposed-jet flames

[1] School of Mechanical Engineering, Purdue University, West Lafayette, Indiana 47907-1288, USA
[2] Department of Mechanical Engineering, University of Connecticut, Storrs, Connecticut 06269-3139, USA

Received: 4 December 2006/Final version: 18 July 2007
Published online: 22 August 2007 •

ABSTRACT A high repetition-rate, two-point, time-resolved, laser-induced fluorescence technique is used to perform simultaneous two-point OH time-series measurements in a series of turbulent opposed-jet partially premixed flames with varying fuel-side equivalence ratio and bulk Reynolds number. Time scales of OH in these flames have previously been reported; however, the extension to two-point detection permits measurements of new spatial and temporal statistics previously unavailable in such flames. In particular, the simultaneous OH time series are used here to compute spatial and temporal autocorrelation functions. Filtered OH length scales ($l_{r,OH}$), corresponding to radial OH fluctuations in turbulent stagnation flames, are obtained from the spatial autocorrelation function, including their variation across the stagnation plane. In general, maximum OH fluctuations occur at the stagnation plane, thus minimizing the OH integral length scale at the axial location of peak OH. For all flames of this study, trends in OH length scale follow those of axial time scale ($\tau_{I,OH}$). For flames with constant Re, $l_{r,OH}$ decreases with less partial premixing. However, this change in integral length scale appears to be more significant for flames at lower Re in comparison to those at higher Re. Similar to OH integral time scales, for flames with the same fuel composition, $l_{r,OH}$ decreases with increasing Re. Moreover, fuel-lean mixtures appear to be more sensitive to Re variations as compared to fuel-rich mixtures.

PACS 47.70.Pq; 32.50.+d; 47.27.wg

1 Introduction

In the context of non-reacting, turbulent, stagnation-point flows, Taylor's hypothesis has generally been used to determine integral length and time scales [1, 2]. Length scales for such flows have previously been found to be relatively constant from the nozzle exit to locations farther downstream [1]. However, since Taylor's hypothesis breaks down in low-velocity regions, i.e., near the stagnation plane, knowledge of spatial and temporal structures within the flow becomes crucial for accurate descriptions of flow dynamics and, more importantly, for further understanding of various combustion models [3]. When combustion is established in the vicinity of a stagnation plane, the turbulent structures are accelerated in one direction (radially) and decelerated in the other (axially), depending on local conditions and the specific influence of large thermal gradients [4]. The interpretation of spatial and temporal structures is further complicated by their dependence on both local turbulent Reynolds number and local equivalence ratio, as affected by changes in internal structure and flame thickness.

In the past decade, turbulent opposed-jet flows and flames have been subjected to various experimental and numerical investigations [4–12]. Measurements of scalar dissipation in nonpremixed and partially premixed flames have drawn especially significant attention [5–7, 12–15]. Mixing processes in opposed-jet flames are further complicated by inherent flow fluctuations and flow-field straining. For this reason, a single average scalar dissipation rate cannot fully characterize local conditions; in other words, multiple temporal and spatial parameters are needed to accurately describe the reacting system.

Spectral measurements of velocity [16] along the jet axis, from the nozzle exits to the stagnation plane, suggest invariant structures, highlighting the fact that basic flow scales remain unchanged when approaching the stagnation plane. While integral length scales from stagnation-plate measurements remain invariant, integral time scales typically rise from the nozzle exit to a maximum near the stagnation plane [1]. The presence of enhanced vorticity at locations near the reaction zone, where axial strain and dilatation exhibit local minima [4], indicates that eddies are preferentially generated near the reaction zone, especially at off-axis positions. The spatial and temporal fluctuations of these eddies extend over a wide range of length and time scales, thus necessitating both high-speed and spatially-resolved measurements.

Only a handful of high repetition-rate techniques currently exist which can spatially and temporally resolve flow and flame structures. While such techniques provide valuable qualitative information, they remain limited by specific flow and experimental conditions. Two-point density measurements were undertaken by Ghenai and Gokalp [17] in Bunsen-type premixed flames, leading to an analysis of time and length scales for the associated scalar field, including mean convection velocities of turbulent scalar structures. Kojima et al. [18] utilized multi-point, time-series measurements

✉ Fax: +1-765-494-0539, E-mail: kvenkate@ecn.purdue.edu

of chemiluminescent signatures to analyze flame-front movement. Since chemiluminescence provides only qualitative information, OH chemiluminescence would not be a suitable indicator of local combustion.

High-speed tomography, together with sophisticated analytical procedures, has previously been used to study the temporal evolution of various flame properties [19–22]. High repetition-rate PLIF imaging at several kilohertz has also been applied to turbulent nonpremixed flames [23, 24]. Recently, Wang et al. [25] conducted high repetition-rate, two-point, laser Rayleigh thermometry in a turbulent nonpremixed jet-flame, thus obtaining thermal power spectra and dissipation rate statistics. However, to date, no measurements detailing the physics of length- and time-scale variations exist for reactive scalars in stagnation-point flames.

Information on minor species, such as the hydroxyl radical, can be used to extract mixture-fraction time scales by using a time-series simulation based on state relationships for laminar flamelets [26]. Indeed, OH time scales in both nonpremixed and partially premixed opposed-jet flames have previously been employed to extract mixture-fraction time scales using a laminar flamelet-based, time-series simulation [26, 27]. From such simulations, relevant OH time scales have been shown to be very sensitive to the OH layer width and movement, but relatively insensitive to quantitative OH concentrations [28]. On this basis, OH time-series statistics in nonpremixed flames are expected to be indicative of overall flame motion. In this study, simultaneous length and time scales of OH, representing flame-front dynamics in stagnation flames, are determined for the purpose of analyzing the response of spatial and temporal structures to changes in both fuel-side equivalence ratio and Reynolds number.

2 Burner and flame configuration

The measurements reported in this paper employed the same burner and flame conditions as reported by Geyer et al. [5, 6]. The flow configuration consists of two identical opposed nozzles inside two opposed annular sections. Each contoured nozzle, with a contraction ratio of 9 : 1, is followed by a straight tube of length 50 mm. The diameter of the inner flow nozzle is 30 mm and that of the co-flow annulus is 60 mm. The annular section outside the inner nozzle provides a flame-stabilizing nitrogen curtain, which prevents reaction of partially premixed fuel before the stagnation plane. The lower and upper nozzles are located at $z = -15$ mm and $z = +15$ mm, respectively. The gaseous flow through each inner nozzle is made turbulent by being passed through perforated plates having hexagonally arranged round holes with a blockage ratio of 45% and a hole diameter of 4.0 mm. The perforated plates are placed 50 mm before the nozzle exits so that the flow is nearly isotropic upstream of the nozzles but anisotropic within the ensuing stagnation flow owing to the developing velocity field [5].

The flow parameters for the partially premixed flames of this study are shown in Table 1. Flames TOJ1A, TOJ1C, TOJ2C and TOJ3C have previously been investigated by employing simultaneous OH PLIF/PIV/PTV [4], OH PLIF [8] and single-point PITLIF [27], respectively. However, PITLIF data for flames TOJ2A, TOJ3A, TOJ1B, TOJ2B, TOJ3B, TOJ2ID and TOJ3ID have not been reported elsewhere. The integral length scale for the velocity field exiting the burner is estimated to be 3.8 mm based on hot-wire anemometry and Taylor's hypothesis, which is nearly the same as the holes in the perforated plate [4–6]. The bulk Reynolds number is calculated based on the exit velocity of the oxidizer jet and the inner nozzle diameter. The bulk strain rates are calculated from the bulk velocities at the nozzle exits. Hence, they are not necessarily equal to the instantaneous local strain rates [4]. However, in this study and also in previous studies involving similar flames [4–8, 27], the bulk strain rate is simply used to characterize various flame configurations based on their flow rates.

Flame	ϕ_B	Re	Bulk velocity ($m\,s^{-1}$)	Bulk strain rate, SR (s^{-1})	Flow residence time (ms)	Minimum OH integral time scale (ms)
TOJ1A	3.2	3300	1.7	117	8.5	7.60
TOJ2A	2.0	3300	1.7	117	8.5	8.70
TOJ3A	1.6	3300	1.7	117	8.5	9.20
TOJ1B	3.2	4100	2.1	142	7.0	6.00
TOJ2B	2.0	4100	2.1	142	7.0	6.75
TOJ3B	1.6	4100	2.1	142	7.0	7.80
TOJ1C	3.2	5000	2.55	175	5.7	5.10
TOJ2C	2.0	5000	2.55	175	5.7	5.25
TOJ3C	1.6	5000	2.55	175	5.7	5.47
TOJ2ID	2.0	6000	3.1	210	4.8	4.55
TOJ3ID	1.6	6000	3.1	210	4.8	5.10

TABLE 1 Flow parameters for the partially premixed flames of this investigation. The bulk Reynolds number and strain rate are defined based on the oxidizer exit velocity. The flow residence time is defined as the reciprocal of the bulk strain rate

3 Experimental procedures

3.1 *Laser system*

The two-point OH time-series measurements were obtained via a two-point version of picosecond time-resolved laser-induced fluorescence (PITLIF) [3, 26]. The laser system used for two-point PITLIF is identical to that employed by Renfro et al. [28]. Briefly, a continuous wave, multimode, argon-ion laser was used to pump a mode-locked Ti:sapphire laser at 16 W. The output of the Ti:sapphire laser consists of 2 ps pulses (FWHM) with a repetition rate of 80 MHz and an average power of 1.3 W. These IR pulses were frequency tripled to produce a final output with a wavelength of 306.5 nm (0.3 nm FWHM) and an average power of 20 mW. The laser was focused within the turbulent flame between the nozzles and excited multiple spectral lines centered near the $R_1(11)$ transition in the $X^2\Pi - A^2\Sigma(0, 0)$ electronic system of OH. This wavelength was selected so that the change in Boltzmann fraction was less than 5% over a range of 1000–2500 K [29].

3.2 *Two-point optical detection*

The objective of two-point detection is to simultaneously image fluorescence signals from two points in space, using separate photomultiplier tubes (PMTs) and gated photon-counting channels [30]. A diagram of the optical detection system is shown in Fig. 1. Photons from two probe

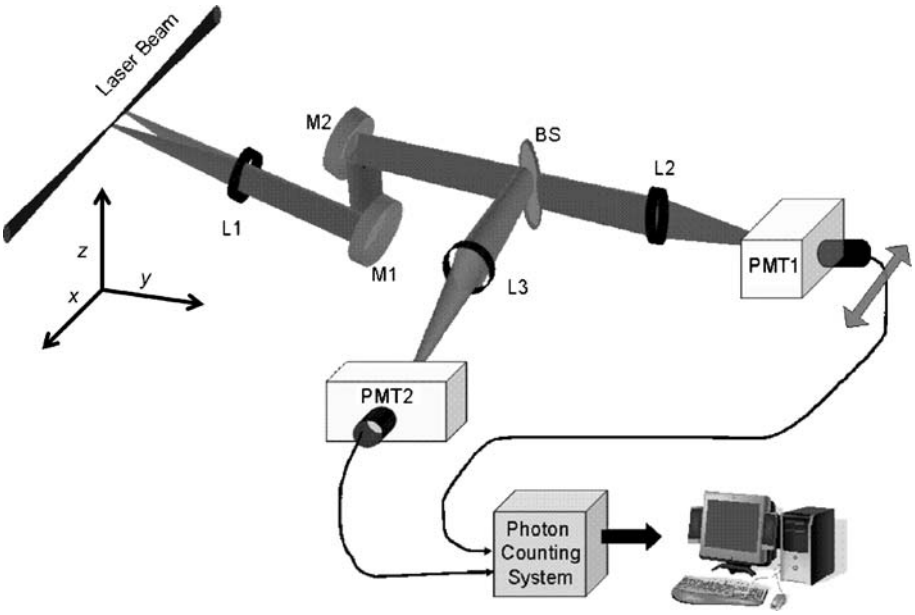

FIGURE 1 Optical detection system for two-point PITLIF. L1 is a 5.0 cm diameter aspherical lens; M1 and M2 are two 7.5 cm UV reflecting mirrors; BS is a 10 cm diameter UV beamsplitter; L2 and L3, L4 and L5 are two pairs of 5.0 cm diameter standard plano-convex and meniscus lenses. PMT1 and PMT2 are 1/8 m monochromators with attached photomultiplier tubes

volumes along the laser beam are collected at right angles to the laser beam by a UV lens (L1). The collimated beam is then passed though a periscope arrangement consisting of two 7.5 cm UV mirrors, split by a beam splitter (BS), and subsequently refocused by uncemented doublets (L2 and L3; L4 and L5) onto corresponding monochromators and PMTs (PMT1 and PMT2) mounted on translation stages. Translating PMT1 while keeping PMT2 stationary moves the imaged probe volume of PMT2 relative to that of PMT1 along the laser beam. The dimensions of the probe volumes are both $250 \times 250 \times 220\,\mu m^3$, as defined by the laser-beam diameter (e^{-2}) and the widths of the monochromator entrance-slits. The wavelength range for the detected fluorescence is selected via two 1/8 m monochromators, which are centered at 306.5 nm with a 10 nm spectral window.

Optical systems involving spherical reflecting or refracting surfaces are often plagued by optical aberrations. Excessive aberrations typically degrade image quality and lead to limited spatial resolution. For two-point detection, partial overlap may arise between the aberrated images of two well-separated probe volumes. This overlap creates artificial coherence between signals from the two probe volumes. A reliable specification to evaluate optical aberrations is the radius of a circle enclosing a certain percentage of the energy passed from a point object [31]. Figure 2 displays such radii corresponding to 80% energy, as determined for our detection system via ZEMAX software [32]. Further analysis suggests that the first lens plays the most important role in determining overall performance and that spherical aberrations are indeed dominant, as demonstrated by the spot diagrams of Fig. 2 [33].

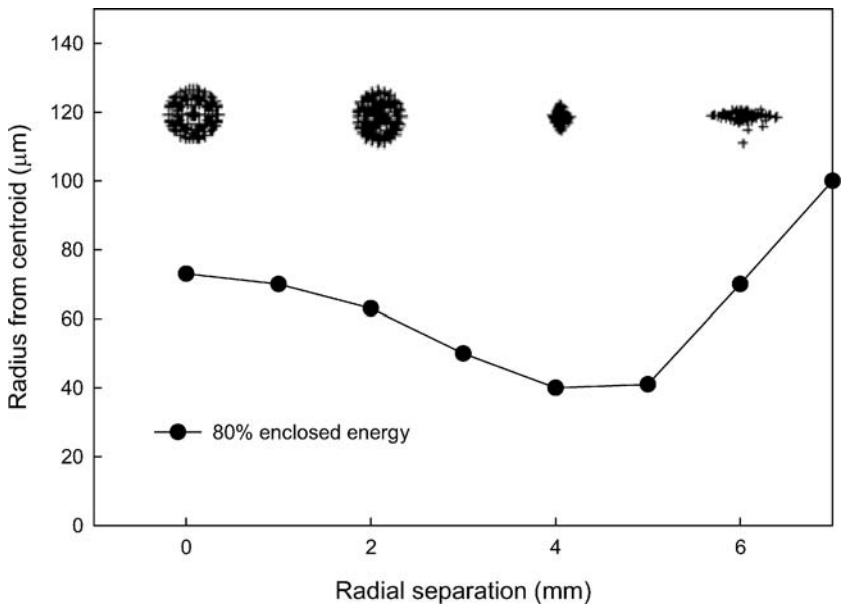

FIGURE 2 Radii of circles enclosing 80% of the total energy for the current optical system. Spot diagrams of the imaged object points are also shown at 0, 2, 4, and 6 mm distances from the optical axis

To resolve integral length scales in the chosen turbulent flames, the separation distance between the two probe volumes was required to be as high as 6 mm. An improved detection system was designed using ZEMAX software to minimize optical aberrations for object points located up to 6.0 mm from the optical axis [32, 33]. The optical system was composed of one custom-made aspherical lens (L1), two 7.5 cm diameter UV reflecting mirrors (M1 and M2), a 10 cm diameter UV beamsplitter (BS), and two pairs of standard plano-convex and meniscus lenses (L2 and L3; L4 and L5). The system produces an aberration-limited blur-spot of less than 140 μm when using a criterion of 80% enclosed energy (Fig. 2). This setup has an optical magnification ratio of 1.2 and a working f# of 2.8.

As the UV optical system was optimized for minimal aberrations at 306.5 nm, the performance of the system must be addressed when considering a 10 nm detection window. In particular, the spot size radius for both the upper and lower limits of the detection band was computed separately using ZEMAX. For the entire detection band, the variation in spot size was $\sim 40\,\mu$m, which is much smaller than the dimensions of the probe volume. Since Fig. 2 results from an optimization using ZEMAX, any alignment error may also affect system performance. In order to overcome the difficulty in performing detailed independent optical aberration calibrations, the alignment of the optical system was indirectly verified by performing two-point measurements on a standard flame (TOJ2C, Table 1) and comparing to previous single-point measurements. Venkatesan et al. [27] obtained single-point radial time scales by translating the burner while maintaining a stationary optical detection system. However, the radial time scales for the current system were obtained by translating one of the two PMTs along the radial direction. As the image point at various radial locations of the translated PMT are affected by aberrations, a direct comparison of the time scales from the current measurements with those of Venkatesan et al. [27] would be a reasonable indicator of the overall effect of the optical aberrations within the measured radial range. The integral time scales for various radial separations of the translated PMT was compared with single-point measurements [27] and the current time scales were found to be repeatable to within 5% of the previous measurements.

The photon-counting system for two-point PITLIF is built along the triple-bin integration method, as developed by Pack et al. [34] and Renfro et al. [35]. In essence, the fluorescence signal following every laser pulse can be approximated by a single exponential decay accompanied by constant background from flame emission. The temporal fluorescence signal from each PMT is divided into three 3.5 ns gated bins (D2, D3 and D4) locked to the arrival time of the laser pulse. Photon counts in each bin are integrated over the sampling interval to produce three simultaneous time series. The required instrumentation, a wiring diagram and a detailed description of the photon-counting process are provided by Zhang et al. [33]. For each PMT, the flame emission counts (D4) are subtracted from the overall signal counts (D2) to yield the corresponding fluorescence signal. Hence, fluorescence time series with suitable background subtraction can be used to compute various two-point statistics, as described subsequently.

The system can be sampled at rates as high as 20 kHz, thus providing a temporal resolution of 50 μs. However, the sampling rate for the current measurements was 2 kHz. For each flame, the sampling rate can be chosen by computing a power spectrum from the measured time series and identifying the highest frequency beyond which spectral rollover occurs. For all flames investigated in this study, a sampling rate of 2 kHz was sufficient to resolve relevant scales, especially as the integral time scales for our flames varied between 3 and 10 ms [27].

3.3 *Data post-processing*

For two simultaneous time series, the space-time correlation function is defined as

$$f_{\mathrm{st}}(\Delta r, \Delta t) = \frac{\left\langle \mathrm{OH}'(r,t)\mathrm{OH}'(r+\Delta r, t+\Delta t)\right\rangle}{\left[\left\langle \mathrm{OH}'(r,t)^2\right\rangle \left\langle \mathrm{OH}'(r+\Delta r, t+\Delta t)^2\right\rangle\right]^{1/2}}\,, \quad (1)$$

where $\mathrm{OH}'(r,t)$is the fluctuating component of OH concentration at radial location r and time t, while Δr and Δt are the radial displacement and time delay, respectively. The spatial correlation coefficient for two simultaneous time series is obtained by setting $\Delta t = 0$ in (1), which thus corresponds to the peak value of the space-time correlation function for a particular radial separation. For scalar measurements, the spatial correlation coefficient is a good indicator of the distance over which turbulent motion at one point is significantly correlated to that at another point [17]. The spatial correlation coefficient typically varies between unity, for two perfectly overlapping time series, and zero, for two completely uncorrelated time series. The spatial autocorrelation function is found by plotting spatial correlation coefficients for various radial separations, i.e.,

$$\begin{aligned} f(\Delta r) &= f_{\mathrm{st}}(\Delta r, \Delta t = 0) \\ &= \frac{\left\langle \mathrm{OH}'(r,t)\mathrm{OH}'(r+\Delta r, t)\right\rangle}{\left[\left\langle \mathrm{OH}'(r,t)^2\right\rangle \left\langle \mathrm{OH}'(r+\Delta r, t)^2\right\rangle\right]^{1/2}}\,. \end{aligned} \quad (2)$$

The integral length scale, obtained by integrating the spatial autocorrelation function over all radial distances, is defined as

$$l_{\mathrm{t}} = \int f(\Delta r)\,\mathrm{d}r\,. \quad (3)$$

The statistical errors for PITLIF length and time scales were estimated using a bootstrap analysis [36]. Each measured time series consisted of 4096 data points which were sampled at 2 kHz. To reduce statistical uncertainty, 30 such time series were obtained over a period of 60 s. The standard deviation of bootstrap replications (i.e., length and time scales), obtained from each time series, provided an error estimate of ±20% at the 95% confidence level.

4 Results and discussion

4.1 *Empirical influences on space-time statistics*

Previous single-point, time-series measurements of radical species in various turbulent nonpremixed flames have shown that mean concentrations and probability density functions (PDFs) are significantly affected by fluctuations

in fluorescence lifetime [35]. However, such lifetimes typically produce negligible effects on quantitative measurements of power spectral densities (PSDs), temporal autocorrelation functions and thus integral time scales [35]. Similarly, the influence of fluorescence lifetime on two-point statistics, particularly the spatial autocorrelation function, were recently investigated for a turbulent jet diffusion flame [33]. The conclusion from this study is that fluctuations in fluorescence lifetime are unimportant for determining spatial statistics related to the concentration field.

Adequate resolution of important frequency components in turbulent flows, along with sufficient signal levels to provide reasonable statistics, necessitate an optimal sampling rate. To resolve the smallest temporal scales, the sampling rate should ideally be as high as possible. However, the maximum sampling rate is limited by signal-to-noise (SNR) considerations. According to Zhang et al. [30], the SNR for PITLIF measurements in the photon-counting mode can be expressed as

$$\mathrm{SNR} = \frac{\sqrt{N_s}}{\sqrt{1+2/\mathrm{SBR}}}, \tag{4}$$

where N_s is the average number of signal photons per sample and SBR is the signal-to-background ratio, defined as the ratio of mean signal to average background photons originating from flame emission. The sampling rate used in our experiments is 2 kHz and the SBR for most of the flames is around two. Typical signal counts per sample in the opposed-jet flames, for both on- and off-axis locations, were from 30 to 100, which lead to corresponding SNRs in the range 4–7. Zhang et al. [33] investigated the effects of under-sampling on the spatial autocorrelation function and found that a smaller sampling rate produced a slightly slower decay owing to time averaging; however, this effect can be deemed negligible. Hence, for the flames of this study, we conclude that the chosen sampling rate plays a relatively unimportant role in determining spatial statistics.

The fluorescence signal can be taken as proportional to peak laser power within the probe volume. Figure 3a shows the fluorescence signal and spatial correlation coefficient as functions of mean laser power at the probe volume for flame TOJ2C. As expected, the fluorescence signal rises nearly linearly with increasing average laser power. At lower laser powers, the photon counts in all bins are dominated by flame emission, leading to a lower correlation coefficient between the simultaneous time series. To avoid this problem, the average laser power for all measurements reported in this study was selected to be ~ 20 mW. The photon counts represented

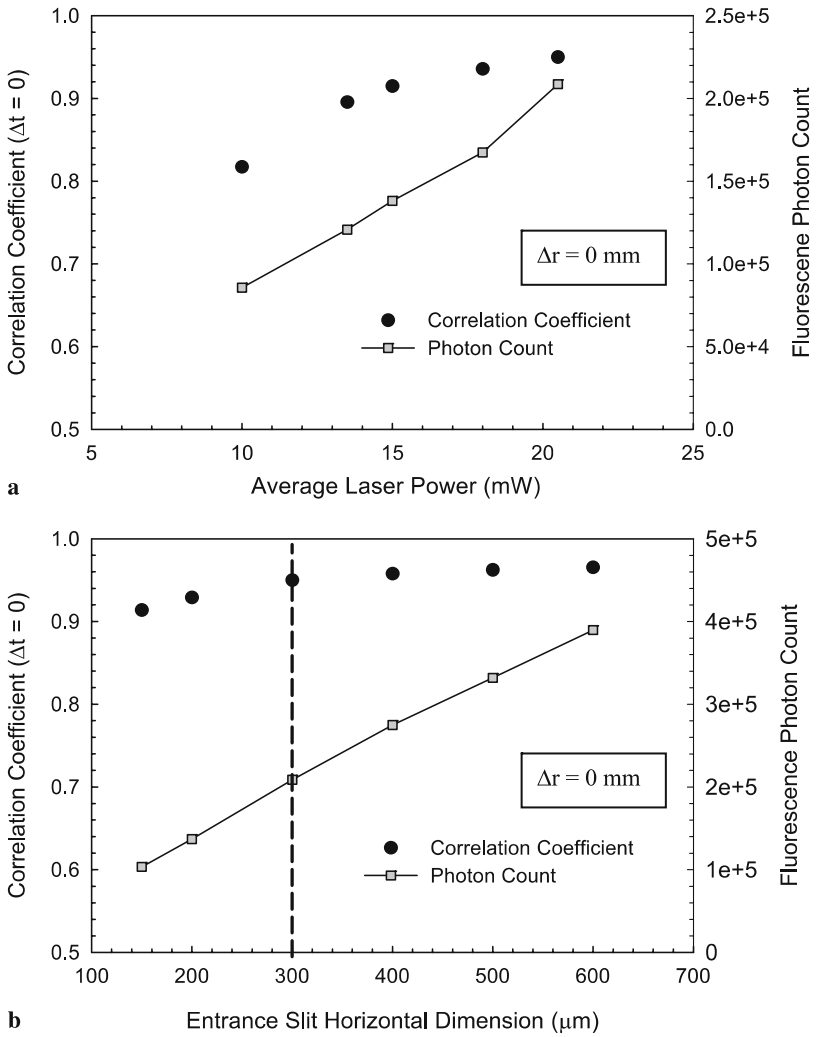

FIGURE 3 Variation of fluorescence photon count and spatial correlation coefficient with (**a**) average laser power at probe volume and (**b**) entrance slit width. The *dashed line* represents the optimal slit width, which produces an average signal photon count of 2*E*5 and a corresponding peak correlation of 0.96. These measurements were performed at the axial location of peak [OH] for flame TOJ2C

by Fig. 3a are obtained by integrating corresponding counts from 2000 data points originally sampled at 2 kHz. Depending on flame conditions, typical average photon counts per sample varies between 30 and 100. Hence, for a laser power of 20 mW, the average photon count per sample is ~ 100, which results in an overall photon count per second of 2×10^5. In addition, the variation in average laser power for consecutive time-series measurements was found to be less than 3%. Hence, based on Fig. 3a, the effect of fluctuations in laser power can be taken as negligible.

The spatial resolution of the detection system depends on the laser beam waist and the horizontal dimension of the entrance slit. The minimum dimension chosen for the entrance slit was based on the average number of signal photons and the degree of correlation between two simultaneous time series. Figure 3b shows the variation in fluorescence signal and spatial correlation coefficient for various entrance slit widths. An increase in slit width from 150 to 600 μm produces a corresponding increase in fluorescence signal of a factor of four. However, the change in correlation coefficient is rather minimal across the entire range of slit widths. At higher sampling rates, slits widths less than 300 μm exhibited a large reduction in signal counts per sample. Moreover, when the PMT was translated, the signal counts decreased further, thereby tending to increase the effects of noise on signal statistics (owing to lower SNRs). Hence, an entrance slit width of 300 μm (see dashed line in Fig. 3b) was chosen as the optimum horizontal dimension for the current measurements.

4.2 *Time-series statistics*

Figure 4 shows time series obtained within flame TOJ2C at the axial location of peak OH for various radial displacements of PMT1 relative to PMT2. When the two probe volumes overlap, the corresponding time series are essentially identical (although small differences arising from noise result in the non-unity correlation coefficients reported in Fig. 3). With increasing separation between the two PMTs, the structures in the two time series diverge from one another, as the local flame front responds to local fluctuations. For the

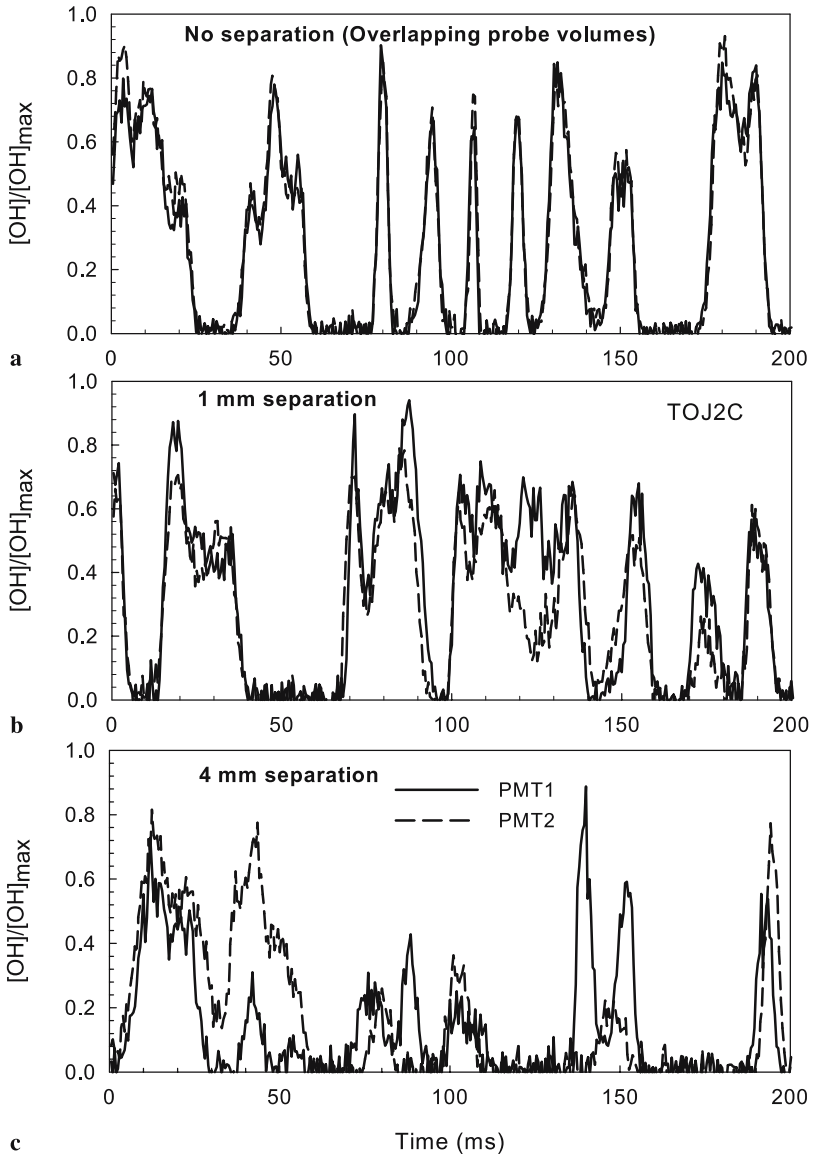

FIGURE 4 Representative two-point OH time series for flame TOJ2C at the axial location of peak [OH] with (**a**) overlapping probe volumes, (**b**) 1 mm separation between probe volumes, and (**c**) 4 mm separation between probe volumes

flame in Fig. 4, as discussed subsequently, the range of integral length scales across the OH layer is between 3 and 5 mm. Hence, when the two probe volumes are separated by 1 mm, as displayed in Fig. 4, the two time series show similar trends and the correlation is visually apparent. For the time series separated by 4 mm, however, local structures monitored by one PMT are absent or only partially visible by the other.

Hydroxyl time series in turbulent flames are usually dominated by intermittency effects [27, 37]. The successive bursts in OH time series can be considered as successive flamelet crossings so that various burst statistics can be used to investigate flamelet dynamics [27]. Statistical analysis of OH time series provide essential information on flame-front fluctuations for a turbulent nonpremixed flame, including especially corresponding time scales characteristic of the flame front. In the flamelet regime, such fluctuations can be related directly to the temporal statistics of flamelet mixture fraction [27, 35]. From these statistics, hydroxyl fluctuations representing large scale flame motion can be characterized by the OH integral time scale. In particular, single-point autocorrelation functions and PSDs are found to be self-similar when normalized by their respective integral time scales [3]. For this reason, given the OH integral time scale and a single normalized PSD, temporal fluctuations in [OH] can be characterized for a large range of flames with both Re and ϕ_B varying. Nevertheless, previous work has not yet considered spatial correlation functions and their associated length scales.

The most energetic fluctuations for turbulent flame environments are typically contained in large-scale eddies characterized by the integral length and time scales. In opposed-jet flows, the residence time of the fluid is so short that insufficient time exists for the transfer of energy from large scales to small scales [5]. In the context of opposed-jet flames, the turbulence is thus "young" or "developing" rather than being fully developed [4–8]. Therefore, most of the turbulent energy in grid-generated, opposed-flow turbulence is contained in large scales. This behavior has been verified through previous single-point PITLIF measurements, as hydroxyl PSDs in similar flames were shown to display little variation over a wide range of Re [27]. Hence, it becomes essential to understand not only the temporal but also the spatial behavior of large-scale structures in such opposed flows. The two-point measurements of this investigation resolve both integral length and time scales, thus providing for the first time spatial statistics in addition to previously measured temporal statistics.

Figure 5 displays the radial space-time correlation function for flame TOJ1C, corresponding to the axial location of peak OH. The radial space-time correlation function can be obtained as follows. Initially, the two PMTs are focused with overlapping probe volumes ($\Delta r = 0$) at the axial location of peak OH. The first probe volume is kept fixed while the second is moved radially in steps of 250 μm while conserving axial location. At each radial separation, 30 time series of 4096 points each are collected so that the cross-correlation function from these time series becomes the space-time correlation function at Δr. A similar procedure is followed for obtaining measurements at other axial locations. The space-time correlation at zero separation is identical to the autocorrelation function found from either probe volume and can thus

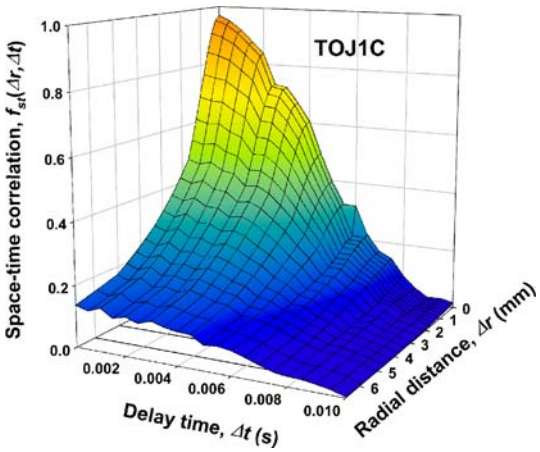

FIGURE 5 Space-time correlation function for flame TOJ1C, measured at the axial location of peak [OH]. Similar results were obtained for all flames of this investigation

be used to determine alternatively the OH integral time scale. As expected, the maximum correlation with successive radial displacement occurs at zero time separation.

The unique feature of the space-time correlation function is the determination of off-axis points which provide simultaneous temporal/spatial information that cannot be obtained from either single-time or single-point data. The space-time correlation function can be decomposed into separate autocorrelation functions for either constant spatial or temporal separation. Autocorrelation functions for various spatial shifts from the space-time plot of Fig. 5 are shown in Fig. 6a. Each curve in Fig. 6a is a slice from the space-time correlation plot for a particular spatial shift. When the autocorrelation functions for various radial shifts are normalized by their respective autocorrelations at zero time delay ($\Delta t = 0$), they essentially collapse onto a single curve for the entire temporal range, as shown in Fig. 6b. In comparison to the temporal autocorrelation functions of Renfro et al. [37], where normalization was performed on both axes, normalization of the current space-time correlation functions is performed only along the y-axis (Fig. 6b). The fact that the correlation coefficient at zero time delay decreases with increasing spatial shift (Fig. 6a) highlights the presence of finite spatial fluctuations spanning the measured radial distance. By normalizing the y-axis in Fig. 6b to unity at zero time delay, the fluctuations for various radial separations are assumed to be completely correlated i.e., they are independent of the various radial separation. If the space-time correlations for the different radial separations are then identical for various temporal separations i.e., if the correlation function collapse onto a single curve, the spatial fluctuations are essentially isolated. This self-similarity indicates that temporal fluctuations are statistically independent of radial shift, i.e., of spatial fluctuations. Therefore, the statistical independence of spatial and temporal fluctuations could conceivably be exploited when specifying such fluctuations in advanced combustion models.

Figure 7 shows the spatial autocorrelation function for flame TOJ2C at peak [OH], fuel-side and air-side locations. The fuel-side and air-side locations are 1.0 mm axially from the peak [OH] location. For overlapping probe volumes ($\Delta r = 0$), the peak cross-correlation coefficient is 0.97. The-

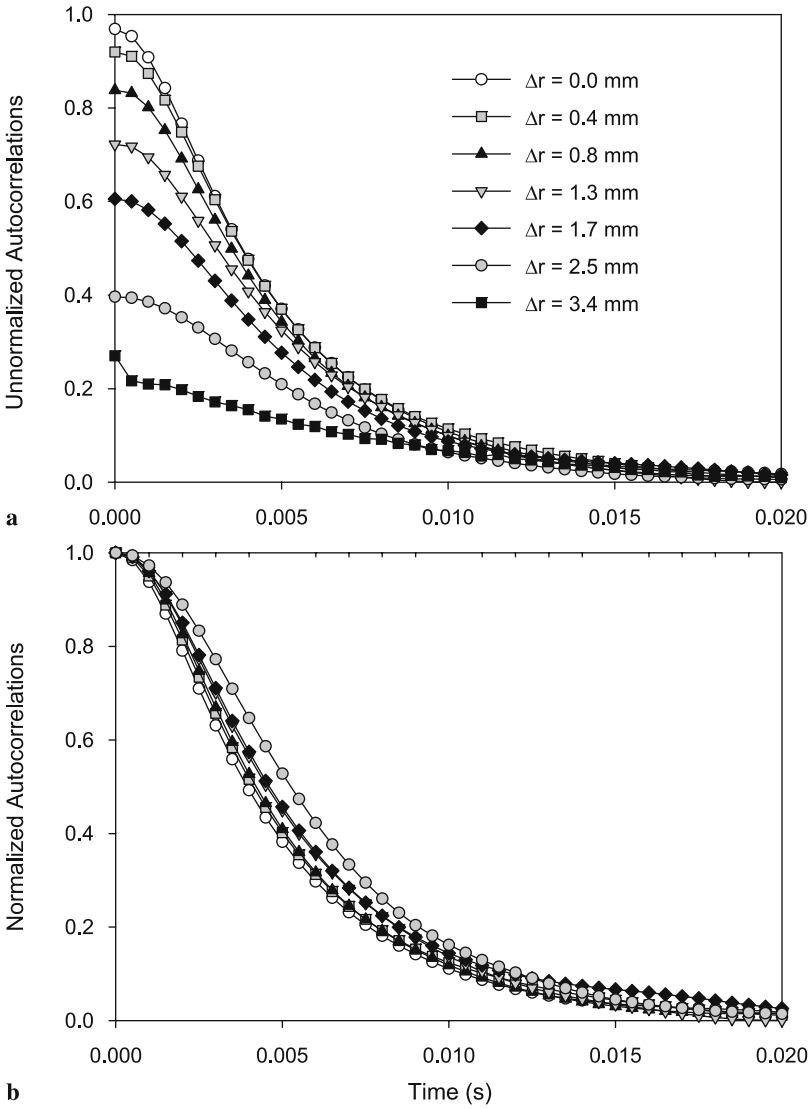

FIGURE 6 Autocorrelation functions for flame TOJ1C at the axial location of peak [OH] for various radial shifts (**a**) unnormalized and (**b**) normalized by the peak correlation at zero time delay

oretically, for identical time series, this correlation coefficient should be unity. However, two simultaneous time series for spatially overlapping probe volumes always display some subtle variations (Fig. 4), often due to a lack of correlation between OH and noise in the time series. In most cases, this defect is quite minor and has little impact on the various two-point, two-time statistics [33]. As shown in Fig. 7, the spatial autocorrelation function at the peak [OH] location displays a faster decay as compared to other locations within the OH layer. This behavior probably arises from an enhanced sensitivity to OH fluctuations at the peak [OH] location.

4.3 *Spatial and temporal scales*

The flames investigated in this paper have previously been shown to fall within the flamelet regime [5]. To bridge our current measurements with the concept of flamelets, we have previously employed time-series simulations using flamelet state relationships for OH to predict mixture-fraction time scales in similar flames [27]. In the context of such a flamelet-based approach, the OH integral time scale gives an indication of the average temporal separation between two consecutive flamelet crossings at a given point within the turbulent flame brush [17]. In this sense, OH integral time scales ($\tau_{I,OH}$) for opposed-jet flames [27] have previously been used to characterize fluctuations within the flame front. Minimal axial OH time scales, obtained from time series having zero spatial separation for all the flames of this study, are listed in Table 1. Flow residence times are also provided, as based on the reciprocal of the bulk strain rate. For flames with fuel-side equivalence ratios, ϕ_B, of 3.2 and 2.0, the minimum OH time scale is almost always a little less than the flow residence time, but these values are quite close and change similarly with Re. This behavior occurs because, in a nonpremixed flame, fluctuations in OH (which represent the flame front) are driven by mixture-fraction fluctuations, which are typically a little faster than those for the accompanying scalar field owing to the narrower width of the OH layer [26]. As measured differences between OH and flow time scales are minimal in these flames, we may conclude that OH fluctuations most likely follow those of the flow field.

The radial variation of OH time scales, corresponding to our three axial positions, is shown in Fig. 8 for flame TOJ2C.

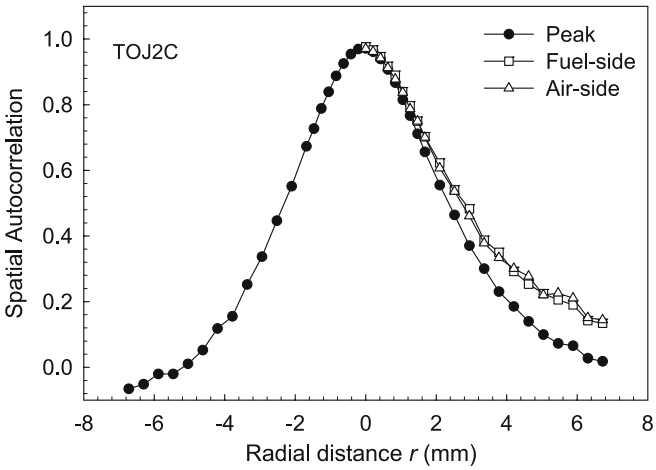

FIGURE 7 Spatial autocorrelation functions for flame TOJ2C at fuel-side, peak [OH] and air-side locations, respectively. The fuel-side and air-side locations are 1 mm from the peak position. For the peak [OH] position, the spatial autocorrelation function is displayed for both the positive and negative radial directions

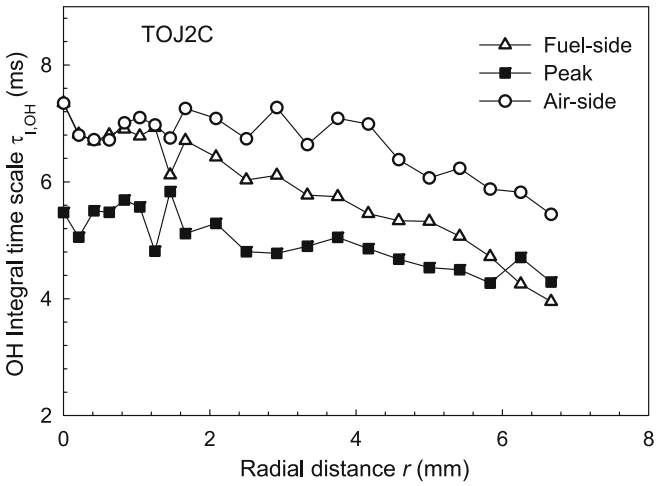

FIGURE 8 Radial variation of OH integral time scale for flame TOJ2C, corresponding to fuel-side, peak [OH] and air-side locations

While these integral time scales could be obtained from single-point measurements, they are nevertheless included in the following discussion to highlight temporal fluctuations in the radial direction and to offer simultaneous comparisons to spatial fluctuations. In general, the integral time scales are relatively lower at the peak [OH] position in comparison to the fuel-side and air-side locations. Conditional flow-field statistics obtained in similar flames [4] indicate that the axial strain at locations upstream of the reaction zone almost always exceeds the radial strain. This feature can be explained by the fact that the time-averaged flame is aligned horizontally, thus driving density gradients mainly in the axial direction. However, near the stagnation plane and at locations close to the OH contours, turbulence is fed from the axial to the radial velocity, thereby increasing radial velocity fluctuations. On this basis, the difference between axial and radial strain diminishes as gas expansion by heat release predominantly accelerates radial velocities. Therefore, along the jet axis, OH fluctuations are larger near the location of peak [OH]. However, because of the above mentioned flow acceleration in the radial direction, higher radial fluctuations could cause larger time-scale gradients, as evident from the fuel-side and air-side time-scale plots in Fig. 8. This behavior is further supported by the fact that, close to the upper and lower regions of the reaction zone, radial velocity fluctuations are higher for off-axis ($r > 0$) locations than along the jet axis [4].

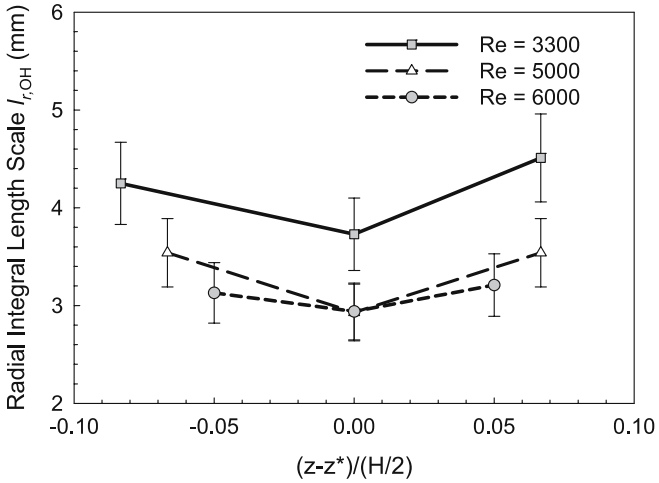

FIGURE 9 Axial variation of OH integral length scale for flames with increasing Re. Each value of the measured length scale is accurate to within ±20% (95% confidence interval of the mean). H represents the nozzle separation distance and z^* represents the axial location of peak [OH]

The influence of turbulence on hydroxyl fluctuations can also be studied by defining a scalar intermittency parameter. This intermittency should not be confused with the usual definition of turbulent intermittency and is defined here as $I(z, t) = \text{Prob}\{[\text{OH}]/[\text{OH}]_{\max} < 0.15\}$, which indicates that $I = 1$ for all time-series data giving $[\text{OH}]/[\text{OH}]_{\max} < 0.15$ and $I = 0$ for all such data giving $[\text{OH}]/[\text{OH}]_{\max} > 0.15$ [27]. For flame TOJ2C, the hydroxyl intermittency is ∼50% for all radial positions corresponding to the location of peak OH. However, because of flow acceleration in the radial direction and its associated fluctuations, the OH intermittency increases to ∼ 65% at radial positions ($r > 0$) corresponding to both fuel-side and air-side locations.

The integral length scale for OH ($l_{\text{r,OH}}$) along the radial direction is obtained by numerically integrating the spatial autocorrelation function. For the flames reported in this study, the spatial autocorrelations are typically composed of 20 points encompassing a separation of 6 mm, so that the length scale is calculated by integrating over this range. Figure 9 shows the axial variation of integral length scale for flames at various Reynolds numbers. In general, $l_{\text{r,OH}}$ is greater at the wings of the OH layer and reaches a minimum at the axial location of peak [OH]. This trend was observed for all flames reported in this study. The axial gradient in OH length scale, across the flame front, decreases with increasing Reynolds number. This effect is highlighted in Fig. 9 as $l_{\text{r,OH}}$ at both fuel- and air-side locations seems to approach $l_{\text{r,OH}}$ values at peak [OH] with increasing Re. This behavior is likely due to less axial variation in turbulence structure with decreasing residence time, and is consistent with previous observations of "young" turbulence in opposed-jet flows [5].

The validity of Taylor's hypothesis near the flame front can be assessed by using simultaneously measured length and

TABLE 2 Hydroxyl and velocity statistics for different axial locations along the jet centerline in flame TOJ2C. †The total velocity is used instead of its radial component because flow symmetry dictates that the radial velocity along the jet centerline is essentially zero [4]. The fuel- and air-side locations are separated from the peak by 1 mm

Axial positions ($r = 0$ mm)	Measured OH length scale, l_{OH} (mm)	Measured OH integral time scale, τ_{OH} (ms)	Total velocity, V (m/s) [4]	Integral time scale from Taylor's hypothesis (l_{OH}/V)
Fuel-side	3.54	6.75	0.175†	20.2
Peak	2.93	5.40	0.075†	39.1
Air-side	3.54	6.75	0.225†	15.7

TABLE 3 Hydroxyl and velocity statistics for different axial locations at $r = 4$ mm in flame TOJ2C. ‡The radial velocity at the peak of the OH front is obtained by assuming a 20% increase above the fuel-side velocity. This increase is identical to those reported for similar flames not investigated in this study [4]. The fuel- and air-side locations are separated from the peak by 1 mm

Axial positions ($r = 4$ mm)	Measured OH length scale at $r = 0$ mm, l_{OH} (mm)	Measured OH integral time scale, τ_{OH} (ms)	Radial velocity, V (m/s) [4]	Integral time scale from Taylor's hypothesis (l_{OH}/V)
Fuel-side	3.54	5.77	0.60	5.9
Peak	2.93	4.90	0.70‡	4.2
Air-side	3.54	7.00	0.40	8.9

TABLE 4 Mean OH speed at various axial positions for flames at different fuel-side equivalence ratios and Re. The fuel-side and air-side locations are located 1.00 mm on either side of the axial [OH] peak

Flame	ϕ_B	Re	Mean OH Speed u_{OH} (m s^{-1})		
			Fuel-side	Peak	Air-side
TOJ2A	2.0	3300	0.42	0.43	0.45
TOJ2B	2.0	4000	–	0.48	–
TOJ2C	2.0	5000	0.52	0.54	0.52
TOJ2ID	2.0	6000	0.59	0.64	0.60
TOJ1A	3.2	3300	0.39	0.40	0.38
TOJ1B	3.2	4000	–	0.50	–
TOJ1C	3.2	5000	0.54	0.55	0.53

time scales [4]. To facilitate this assessment, flame TOJ2C was chosen, as previous velocity statistics are available for this flame via the flow field measurements of Böhm et al. [4]. The integral time scales computed using Taylor's hypothesis, for different axial positions corresponding to two different radial locations, are compared to PITLIF time scales in Tables 2 and 3. For axial locations along the jet centerline (Table 2), a large deviation exists between the calculated and measured time scales. We note that, mean velocities near the stagnation point are negligible causing a large uncertainty in their estimation. Moreover, Taylor's hypothesis ignores velocity fluctuations. Hence, as expected, Taylor's hypothesis fails for locations along the jet axis in opposed-jet flows. For off-axis locations, however, good agreement prevails between measured and computed time scales, as shown in Table 3. Since, the flow is predominantly radial at off-axis locations, the acceleration induced by heat release creates a shear-layer effect which is well represented by the mean convection. Therefore, for reacting turbulent opposed-jets, Taylor's hypothesis tends to be valid for off-axis locations, as compared to locations along the jet centerline. Previous studies in a self-preserving region of a circular jet have shown that the Taylor's hypothesis is applicable only along the jet axis [38, 39]. Because these studies were conducted at regions where the turbulence intensity is relatively high and where the local isotropy is approximately satisfied in the fully developed region, their applicability to the current weakly turbulent and developing flames can only be approximate. Nevertheless, our results are consistent with those of Mi and Antonia [38] and Dahm and Southerland [39] in highlighting that the Taylor's hypothesis is indeed invalid at locations (i.e., near the stagnation point [4]) where the turbulent intensities are relatively higher.

A mean OH speed (u_{OH}) can be defined by taking the ratio of OH length scale ($l_{r,OH}$) to OH time scale ($\tau_{I,OH}$). Large-scale OH structures can be assumed to be convected at this mean speed over locations spanning the size of these structures. The axial variation of u_{OH} for various flames is shown in Table 4. The fuel-side and air-side locations are again at a distance of 1 mm from the peak [OH] position. In general, the mean OH speed remains constant across the flames but rises with increasing Reynolds number. As shown in Fig. 10, for flames with the same bulk Reynolds number, the OH integral length scale decreases with increasing fuel-side equivalence ratio (or reduced partial premixing). Single-point, time-series measurements in similar flames, previously reported

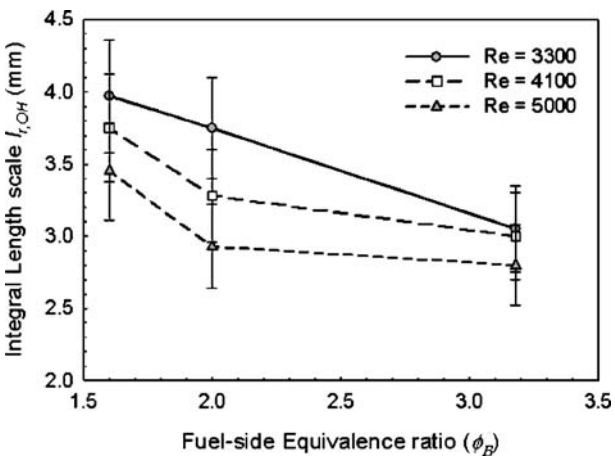

FIGURE 10 Variation of OH integral length scale with fuel-side equivalence ratio (ϕ_B) at constant Re. Measurements were obtained at the axial location of peak [OH] for the corresponding flames

by Venkatesan et al. [27], show that flames at higher equivalence ratios have greater OH intermittencies and thus shorter bursts. These shortened bursts represent a thinner flame front and thus are subject to larger fluctuations for similar upstream flow conditions. However, the change in length scale with varying fuel mixture appears to be more pronounced at lower Reynolds numbers. For higher Re, the length scales are almost constant despite large changes in fuel-side equivalence ratio.

Figure 11 displays the variation of OH integral length scale with Reynolds number for flames having the same fuel-side equivalence ratio. For constant fuel composition, the integral length scale generally decreases with increasing Reynolds number. At lower Re, for which the flow has more time to develop, a nearly linear relationship exists between length scale and Re, similar to the correlation observed by Omar et al. [8] between instantaneous flame width and Re. However, at higher Re, the flow has less time to develop, which leads to an insensitivity between the OH length scale and Re.

We have previously shown that, for turbulent nonpremixed flames, the OH integral time scale decreases with increasing Re [27]. In general, for all flames reported in this study, the trends in integral length scale follow those of time scale. However, with increasing Re, the time scales of Table 1 appear to decrease faster than the length scales of Fig. 11. This behavior is also evident from the u_{OH} values at peak [OH], as shown in Table 4. We note that the Re dependence presented in Fig. 11 is defined based on the bulk velocity owing to difficulties in experimentally determining a local Re. In addition, the trends with Re may be quantitatively affected by heat release; nevertheless, a higher bulk Re will produce a higher local Re, thus still making the qualitative trends relevant.

Since both time and length scales decrease with increasing Re, the faster mean OH speed with increasing Re implies that the time scale decreases faster than the corresponding length scale. This effect probably arises from a convolution of short residence times, reduced width of the OH layer and flow acceleration owing to heat release, which affects temporal fluctuations in the flow far greater than their associated spatial structures. In flames with very high Re, for example, both the changes in length scale across the reaction zone (Fig. 9) and in mean OH speed (Table 4) were found to be negligible, so that flow residence times are almost equal to OH time scales (Table 1). For such cases, the spatial structures are typically convected along the axial direction and across the reaction zone with constant mean velocity; hence, large density gradients appear to have minimal effects on spatial fluctuations of OH structures. This result does not necessarily mean that turbulent structures are 'rigidly' convected with a constant mean velocity. Rather, temporal fluctuations in spatial structures are enhanced owing to flow acceleration and the reduced width of OH layers, as evident from the steep axial [27] and radial gradients in OH time scale, especially displayed for the latter in Fig. 8.

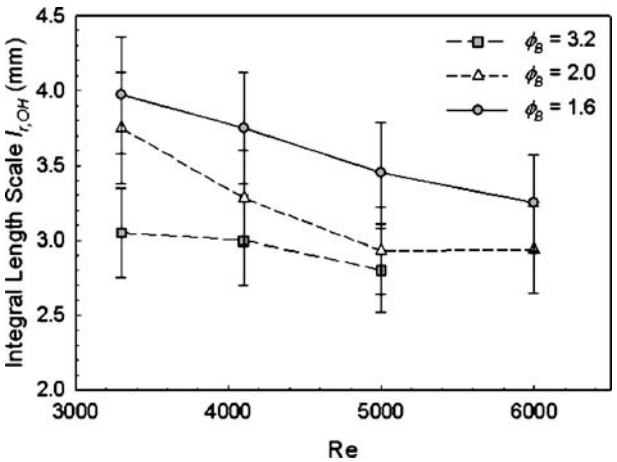

FIGURE 11 Variation of OH integral length scale with Re at constant φ_B. Measurements were obtained at the axial location of peak [OH] for the corresponding flames

5 Conclusions

Simultaneous two-point, time-series measurements of OH were obtained in a set of turbulent partially premixed opposed-jet flames. The optical system has a spatial resolution of $250 \times 250 \times 220\ \mu m^3$ and a temporal resolution of 50 μs, thus permitting complete resolution of both hydroxyl integral length and time scales. The axial and radial variation of hydroxyl temporal and spatial scales are investigated near the stagnation flame front as functions of bulk Reynolds number and fuel-side equivalence ratio. Various two-point statistics such as the space-time correlation function and the spatial autocorrelation function are investigated, and are further used to extract OH integral length and time scales.

In general, the axial variation of radial OH length scale is similar to that of the OH time scale in opposed-jet flames. The axial change in length scale is more pronounced for flames with lower bulk Re and greater partial premixing. The radial length scales are found to decrease with both increasing Re and increasing fuel-side equivalence ratio. For flames of a given fuel composition, the change in length scale from lower to higher Re, at axial locations of peak [OH], appears to be greater for flames at lower fuel-side equivalence ratios. Similarly, for flames at constant Re, the change in length scale from lower to higher fuel-side equivalence ratios appears to be more pronounced at relatively low Re.

The mean OH speed, defined as the ratio of the OH length to time scale, remains almost constant across the reaction zone. For a constant bulk flow Re, the mean OH speed seems to be nearly independent of fuel composition. However, the mean OH speed rises with increasing Re. In comparison to the OH length scale, the OH time scale appears to decrease faster with increasing Re. This result highlights the negligible effect of the reaction zone on spatial OH fluctuations but its enhanced effect on temporal fluctuations owing to flow straining in the axial direction and to flow acceleration arising from heat release in the radial direction.

ACKNOWLEDGEMENTS This project was supported by the National Science Foundation, with Dr. Linda Blevins serving as a technical monitor. We thank Dr. Robert Barlow of the Combustion Research Facility at Sandia National Laboratories, for providing us with the opposed-jet burner used in this study. We also thank Dr. Andreas Dreizler and Dr. Dirk Geyer (Technische Universität, Darmstadt) for their valuable suggestions. We appreciate the help in installing the burner from Mr. Matthew Gluesenkamp.

REFERENCES

1 P. Cho, C.K. Law, R.K. Cheng, I.G. Shepherd, Proc. Combust. Inst. **22**, 739 (1988)
2 R.K. Cheng, I.G. Shepherd, I. Gökalp, Combust. Flame **78**, 205 (1989)
3 M.W. Renfro, A. Chaturvedy, G.B. King, N.M. Laurendeau, A. Kempf, A. Dreizler, J. Janicka, Combust. Flame **139**, 142 (2004)
4 B. Böhm, D. Geyer, A. Dreizler, K.K. Venkatesan, N.M. Laurendeau, M.W. Renfro, Proc. Combust. Inst. **31**, 709 (2007)
5 D. Geyer, A. Kempf, A. Dreizler, J. Janicka, Proc. Combust. Inst. **30**, 681 (2005)
6 D. Geyer, A. Dreizler, J. Janicka, A.D. Permana, J.Y. Chen, Proc. Combust. Inst. **30**, 711 (2005)
7 D. Geyer, A. Kempf, A. Dreizler, J. Janicka, Combust. Flame **143**, 524 (2005)
8 S.K. Omar, D. Geyer, A. Dreizler, J. Janicka, Prog. Comput. Fluid. Dynam. **4**, 241 (2004)
9 R.P. Lindstedt, D. Luff, J.H. Whitelaw, Flow Turbul. Combust. **74**, 169 (2005)
10 A. Kitajima, T. Ueda, A. Matsuo, M. Mizomoto, Combust. Flame **121**, 301 (2000)
11 E. Mastorakos, A.M.K.P. Taylor, J.H. Whitelaw, Combust. Flame **91**, 40 (1992)
12 E. Mastorakos, A.M.K.P. Taylor, J.H. Whitelaw, Combust. Flame **91**, 55 (1992)
13 R.S. Barlow, A.N. Karpetis, Proc. Combust. Inst. **30**, 673 (2004)
14 J.H. Frank, S.A. Kaiser, M.B. Long, Proc. Combust. Inst. **29**, 2687 (2002)
15 S.H. Stârner, R.W. Bilger, R.W. Dibble, R.S. Barlow, Combust. Sci. Technol. **86**, 223 (1992)
16 L.W. Kostiuk, K.N.C. Bray, R.K. Cheng, Combust. Flame **92**, 377 (1993)
17 C. Ghenai, I. Gokalp, Exp. Fluids **24**, 347 (1998)
18 J. Kojima, Y. Ikeda, T. Nakajima, Meas. Sci. Technol. **14**, 1714 (2003)
19 C.J. Dasch, Appl. Opt. **31**, 1146 (1992)
20 K.T. Walsh, M.B. Long, M.A. Tanoff, M.D. Smooke, Proc. Combust. Inst. **27**, 615 (1998)
21 A.J. Marchese, F.L. Dryer, M. Vedha-Nayagam, R. Colantonio, Proc. Combust. Inst. **26**, 1219 (1996)
22 B. Renou, A. Boukhalfa, D. Puechberty, M. Trinité, Combust. Flame **123**, 507 (2000)
23 C. F. Kaminski., J. Hult, M. Aldén, Appl. Phys. B **68**, 757 (1999)
24 A. Dreizler, S. Lindenmaier, U. Maas, J. Hult, M. Aldén, C.F. Kaminski, Appl. Phys. B **70**, 287 (2000)
25 G.H. Wang, N.T. Clemens, P.L. Varghese, Proc. Combust. Inst. **30**, 691 (2005)
26 M.W. Renfro, J.P. Gore, N.M. Laurendeau, Combust. Flame **129**, 120 (2002)
27 K.K. Venkatesan, N.M. Laurendeau, M.W. Renfro, D. Geyer, A. Dreizler, Flow Turbul. Combust. **76**, 257 (2006)
28 M.W. Renfro, W.A. Guttenfelder, G.B. King, N.M. Laurendeau, Combust. Flame **123**, 389 (2000)
29 J. Luque, D.R. Crosley: LIFBASE: Database and Spectral Simulation (version 2.0.2), SRI Int. Report MP 99-009 (1999)
30 J. Zhang, K.K. Venkatesan, G.B. King, N.M. Laurendeau, M.W. Renfro, Opt. Lett. **30**, 3144 (2005)
31 R.E. Fischer, B. Tadic-Galeb, *Optical System Design* (McGraw-Hill, New York, 2000)
32 *Software for Optical Design*, ZEMAX Development Corporation, Bellevue, Washington (2004)
33 J. Zhang, G.B. King, N.M. Laurendeau, M.W. Renfro, Appl. Opt. **46**, 5742 (2007)
34 S.D. Pack, M.W. Renfro, G.B. King, N.M. Laurendeau, Opt. Lett. **23**, 1215 (1998)
35 M.W. Renfro, G.B. King, N.M. Laurendeau, Appl. Opt. **38**, 4596 (1999)
36 B. Efron, R.J. Tibshirani, *An Introduction to The Bootstrap* (Chapman and Hall, London, 1993)
37 M.W. Renfro, S.D. Pack, G.B. King, N.M. Laurendeau, Appl. Phys. B **69**, 137 (1999)
38 J. Mi, R.A. Antonia, Phys. Fluids A **6**, 1548 (1994)
39 W.J.A. Dahm, K.B. Southerland, Phys. Fluids A **9**, 2101 (1999)